EXPERIMENTAL INVESTIGATION OF THE DLR-F23 CONFIGURATION AT TRANSONIC SPEEDS USING FAST-RESPONSE PRESSURE-SENSITIVE PAINT

Patrick Hartl, Maik Ritschel, Marc Braune & Holger Mai

German Aerospace Center (DLR), Institute of Aeroelasticity, Department of Aeroelastic Experiments, Bunsenstraße 10, 37073 Göttingen, Germany, patrick.hartl@dlr.de

Abstract

Modern, high-agility aircraft configurations cover an extensive flight envelope, consisting of flight conditions with high maneuverability at subsonic speeds as well as flight conditions with high-level performance in the transonic and supersonic flow regime. In this study, the DLR-F23 hybrid-delta-wing configuration, consisting of a low aspect-ratio triple-delta-wing planform, is investigated in the Transonic Wind Tunnel Göttingen (DNW-TWG). The measurements are performed at Mach numbers between $Ma = 0.55$ and $Ma = 1.15$ in the angle of attack range from $\alpha = 0^\circ$ to $\alpha = 30^\circ$. Fast-response pressure-sensitive paint measurements (iPSP) are conducted to analyze the aerodynamic surface pressure distribution and the pressure fluctuations. The iPSP measurements are validated with unsteady pressure transducers. A special focus is on the analysis of vortex-vortex and vortex-shock interactions, as well as shock-induced vortex breakdown for three selected cases for subsonic, transonic, and supersonic flow conditions. Proper Orthogonal Decomposition (POD), as an advanced data analysis method, is used to reduce the high-dimensional iPSP data into a series of orthogonal modes arranged according to their energy content. For the subsonic flow case, vortex-vortex interactions can be observed, which results in vortex merging. Shock-induced vortex breakdown is identified in the transonic flow regime. The supersonic case is characterized by multiple vortex-shock interactions. Several strong cross-flow shocks along the vortex trajectories of the primary vortices deeply influence the surface pressure distribution on the wing.

Keywords: Hybrid Delta Wing, Vortex Flow Aerodynamics, Pressure Sensitive Paint, Proper Orthogonal Decomposition

1. Introduction

High-agility aircraft configurations operate under extreme flight conditions, requiring effective supersonic cruise and high maneuverability at subsonic conditions. The necessary agility and speed performance of combat aircraft is achieved by low-aspect-ratio highly swept wings. Over the last few decades, it has been shown that the delta wing planform performs well under these operating conditions. The required flight envelope and mission spectrum of future multi-role combat aircraft lead to developing new configurations with hybrid-delta-wing planforms, consisting of multiple swept leading edges [1]. As a result of the changing requirements for future combat aircraft, stable vortex flows are increasingly gaining importance in aerodynamic design, especially at transonic speeds. The aircraft planform, wing-sweep, and leading-edge shape have to be designed in such a way that these complex flows are mutually beneficial throughout the entire flight envelope [2].

For multiple swept delta-wing configurations, the flow separates at the leading edge at a small to medium angle of attack (AoA), and the shear layer rolls up, forming a leading-edge vortex. These configurations are characterized by a complex flow field consisting of multiple vortices that form a vortex system. The vortices induce a high axial velocity in the vortex core and a suction peak in the surface pressure, which results in a nonlinear, vortex-induced lift increase. These vortices interact

with each other and with shocks that are formed on the upper side of the wing at transonic flow conditions [3]. While vortex-vortex interactions can lead to a stabilizing effect on the vortices involved, vortex-shock interactions have a destabilizing effect and can, therefore, cause shock-induced vortex breakdown [4]. The phenomenon of vortex breakdown can be described by a sudden widening of the vortex itself. It is associated with a reversed flow and strong fluctuations within the vortex core [5, 6]. This results in a loss of suction beginning at the rear part of the wing, but with a further increase in AoA, the breakdown location shifts upstream [7]. As vortex breakdown leads to a sudden reduction of lift, it can induce strong forces and moments, which affect the stability and control characteristics of the aircraft. For this reason, it is essential for the design of aircraft with multiple-swept delta wings to understand the physical phenomena behind these interactions.

At the Institute of Aeroelasticity of the German Aerospace Center (DLR), a new hybrid-delta-wing configuration, the DLR-F23, was developed for the experimental investigation of unsteady flow phenomena associated with leading-edge vortices at transonic flow conditions [8, 9]. The DLR-F23 wing-fuselage half-span wind tunnel model consists of a triple-delta wing with an ogival cosine-chined forebody. For the analysis of unsteady aerodynamics, a more detailed measurement of the surface pressure fluctuations on the upper side of the wing is of high priority. Therefore, the established Pressure Sensitive Paint (PSP) measuring technique was applied. PSP is an optical measurement method for acquiring surface pressure information with high spatial resolution [10]. To determine the surface pressure using this method, the model is coated with a special paint, which is illuminated by UV light. The intensity of the resulting fluorescence light depends on the local oxygen concentration, which allows for determining the two-dimensional pressure distribution. Conventional pressure measurement methods can only measure the pressure distribution at discrete points on the surface by installing pressure sensors such as taps and unsteady pressure transducers, while the two-dimensional PSP method provides a measurement of the overall surface. Furthermore, the PSP technique enables pressure measurement on surfaces without inserting flow-disturbing probes and without affecting the surface of the model. Conventional PSP methods usually only acquire the steady surface pressure distribution. In order to measure unsteady pressure fluctuations, a fast-response pressure-sensitive paint (iPSP) was developed at the DLR based on formulation introduced by Ponomarev and Gouterman [11] and subsequently improved by Gregory et al. [12]. In combination with high-speed cameras, the fast-response, pressure-sensitive paint allows the spatial resolution of conventional PSP to be combined with high temporal resolution.

An overview of the development of pressure-sensitive paint technology as an advanced measurement technique for unsteady aerodynamics is presented in Gregory et al. [13]. Kameda et al. [14] investigated the unsteady pressure distribution on a delta wing with a leading edge sweep of 65° at transonic speeds. The experiment was conducted with a freestream Mach number of 0.90 and an AoA of 20°. The experimental results verified that terminating shock waves moved back and forth due to shock-wave/vortex interaction. Wiggen et al. [15] analyzed the unsteady surface pressure distributions at a pitching Lambda wing for vortex-dominated flow with iPSP measurements and unsteady pressure transducers at transonic flow conditions. The half-span wind tunnel model has a leading edge sweep of 53°. The free stream Mach number was varied between $0.3 < Ma_\infty < 0.7$, and the wing was excited with small pitching amplitudes of $0.08^\circ - 0.40^\circ$ at frequencies up to $40\ Hz$. The evaluation of the iPSP measurements showed that the transonic influences are dominant at small angles of attack, whereas the influence of the vortex system dominates the behavior of the pressure fluctuations at higher angles of attack. Katzenmeier et al. [16] investigated a mixed material, flexible aircraft wind tunnel model with a $76^\circ/40^\circ$ double-delta wing and a horizontal tail plane at subsonic speeds and high angles of attack. The buffeting effects on the configuration are measured with high-speed cameras to simultaneously record the unsteady surface pressures with iPSP and the dynamic three-dimensional structural deformation. The authors developed a post-processing toolchain to automatically analyze the experimental results.

The spatial and temporal resolution capabilities of time-resolved PSP measurements can be significantly improved by using advanced data analysis. Methods such as Proper Orthogonal Decomposi-

tion (POD), Spectral Proper Orthogonal Decomposition (SPOD), and Dynamic Mode Decomposition (DMD) have been developed to extract important flow features and patterns as a compact representation of high-dimensional data. POD describes a decomposition of the data into a series of orthogonal modes based on the spatio-temporal correlation of the measurement data. A POD mode is a left singular vector of the Single Value Decomposition (SVD) and can be calculated with the common SVD algorithm. The POD modes are sorted according to the energy they contain in the original data. A more detailed description of the POD method can be found in Berkooz et al. [17] and Cordier and Bergmann [18].

The present paper is further organized as follows. Section 2 gives an overview of the design of the DLR-F23 configuration with its geometrical parameters. Section 3 describes the wind tunnel facility and the experimental setup, as well as the measurement methods and the measurement conditions. In section 4, the results of the experimental investigation and the iPSP measurements for the subsonic, transonic, and supersonic flow conditions are discussed. The mean surface pressure distributions and the pressure fluctuations from the iPSP measurements on the upper side of the triple-delta wing are analyzed. Subsequently, the local Mach number distribution on the upper side of the wing is evaluated. For a more detailed evaluation of the vortex flow aerodynamics, the surface traces of the vortex trajectories and the corresponding pressure distributions along the vortex trajectories are analyzed. Section 5summarizes the experimental results and gives an outlook.

2. Configuration

A new multi-delta-wing configuration was developed for the DLR project Diabolo, which resulted in the DLR-F23 [8, 9]. The generic wing-fuselage half-span wind tunnel model consists of a triple-delta-wing planform with an ogival cosine-chined forebody. Figure 1 provides an overview of the model from different perspectives and shows the model parameters. The configuration is divided into three wing segments of different leading-edge sweeps. The front wing part, comparable with a leading-edge vortex controller (LEVCON), has a medium leading-edge sweep of $\varphi_{W,1} = 45°$, followed by a wing midsection (strake) with a high leading-edge sweep of $\varphi_{W,2} = 75°$ and the main wing section with the similar leading-edge sweep as the front section, $\varphi_{W,3} = \varphi_{W,1}$. The leading edge of each wing segment has a constant radius of $r_{LE} = 0.50\,mm$. The model consists of elliptic airfoils for each wing section that tapers into a sharp trailing edge (TE) of a height of $0.50\,mm$. The TE of the main wing section has a negative sweep of $\varphi_{W,TE} = -10°$. Figure 1 shows the section views of the elliptical airfoil shape (section A-A) in the junction between the LEVCON and the strake and of the cosine-chined forebody (section B-B).

The dimensions of the DLR-F23 wind tunnel model are summarized in Table 1. The origin of the body-fixed coordinate system is located at the apex of the forebody, as shown in Fig. 1. The configuration has a total length of $l_M = 0.862\,m$ and a half span of $s_M = 0.420\,m$. It has a wing root chord of $c_{r,W} = 0.575\,m$ and a wing tip chord of $c_{t,W} = 0.070\,m$. The mean aerodynamic chord is $l_\mu = 0.382\,m$. In order to specify the thickness-to-chord ratio of the multi-delta wing, four spanwise distributed sections are defined in the front view according to Fig. 1. In section 1 at $y_1/s_M = 0.160$, the thickness ratio of the elliptical airfoil is $t_1/c_1 = 0.077$. For section 2 at $y_2/s_M = 0.355$ at the interface from LEVCON to strake, the relative thickness is $t_2/c_2 = 0.077$. In section 3 at $y_3/s_M = 0.435$ at the transition for the strake segment to the main wing, the thickness ratio is $t_3/c_3 = 0.067$. The relative thickness of the cropped wing tip in section 4 is $t_4/c_{t,W} = 0.084$. The lengths of the LEVCON segment, the strake segment, and the main wing segment are $l_1/c_{r,W} = 0.145$, $l_1/c_{r,W} = 0.210$ and $l_1/c_{r,W} = 0.645$ for each respective section. The wing reference area of multi-delta-wing configurations is usually specified in the literature only with the base trapezoid without the leading-edge extension, as shown in Fig. 1. The wing reference area of the base trapezoid is $A_{ref} = 0.133\,m^2$ and the wing aspect ratio and the taper ratio are $\Lambda = 2.65$ and $\lambda = 0.13$. The wind tunnel model is designed with an integrated peniche with a width of $w_P = 0.03\,m$, shown in Fig. 1, to reduce the influence of the wind tunnel boundary layer on the model.

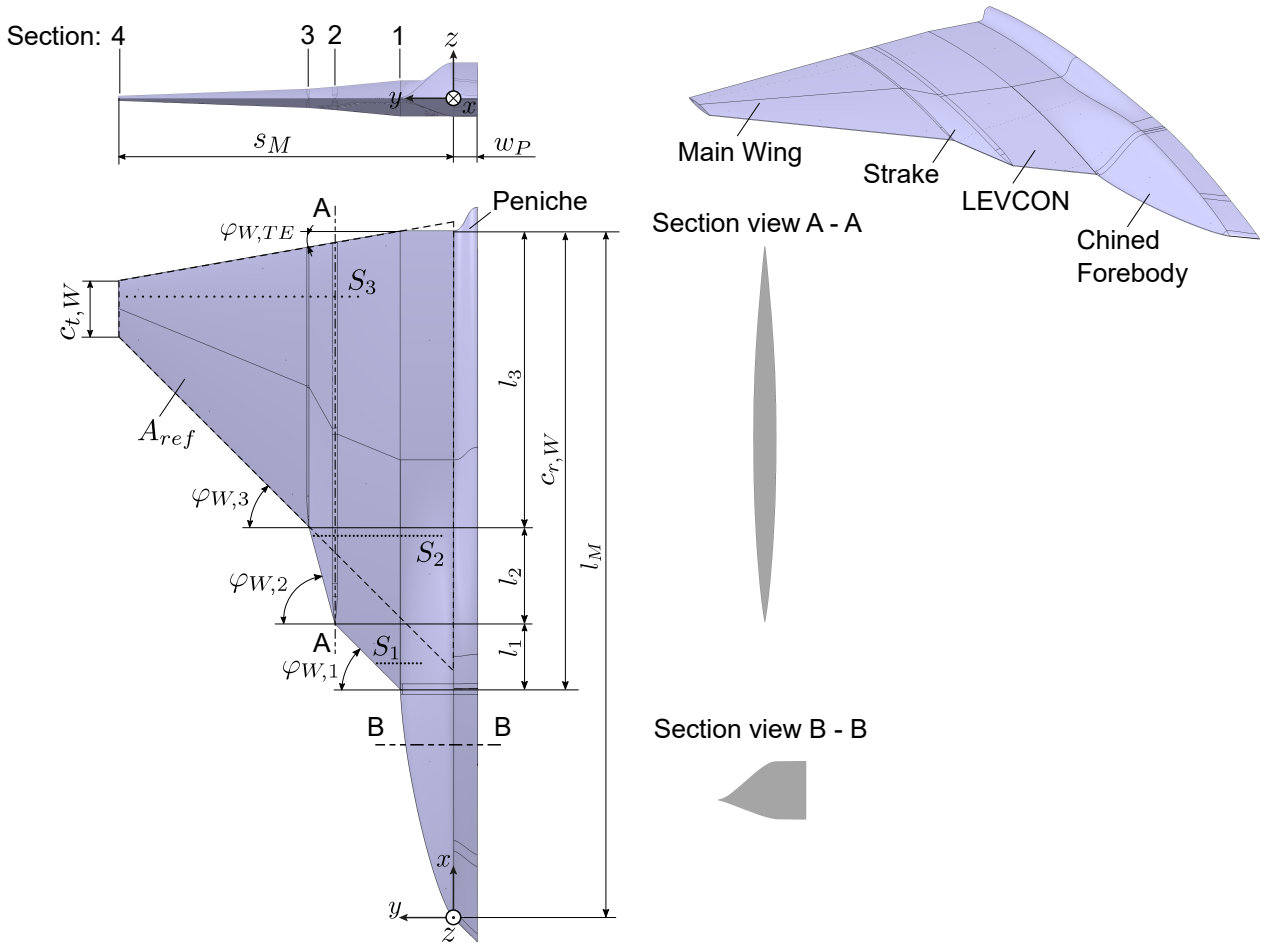

Figure 1 – Geometrical parameters of the DLR-F23 wind tunnel model

Table 1 – Dimensions and characteristic planform parameters of the DLR-F23 wind tunnel model

Geometrial Parameter	
Model length l_M	0.862 m
Model half span s_M	0.420 m
Wing root chord $c_{r,W}$	0.575 m
Wing tip chord $c_{t,W}$	0.070 m
Mean aerodynamic chord l_μ	0.382 m
LEVCON segment length $l_1/c_{r,W}$	0.145
Strake segment length $l_2/c_{r,W}$	0.210
Main wing segment length $l_3/c_{r,W}$	0.645
LEVCON LE sweep $\varphi_{W,1}$	45°
Strake LE sweep $\varphi_{W,2}$	75°
Main wing LE sweep $\varphi_{W,3}$	45°
Trailing edge sweep $\varphi_{W,TE}$	-10°
Wing reference area A_{ref}	0.133 m²
Wing aspect ratio Λ	2.65
Wing taper ratio λ	0.13

3. Experimental Setup

The experimental investigations of the DLR-F23 multi-delta-wing configuration were conducted at the Transonic Wind Tunnel Göttingen (TWG). The measurement campaign mainly focused on the time-resolved pressure-sensitive paint (iPSP) measurements on the upper side of the wind tunnel model. In addition, the model was instrumented with unsteady pressure transducers to investigate the unsteady surface pressures. The following section gives an overview of the wind tunnel facility, the measurement setup, the measurement techniques, and the measurement conditions.

3.1 Wind Tunnel Facility

The measurement campaign was performed at the Transonic Wind Tunnel Göttingen (DNW-TWG), operated by the German-Dutch Wind Tunnels (DNW). Figure 2 shows a schematic representation of the DNW-TWG. The closed-circuit Göttingen-type wind tunnel allows continuous inflow in the subsonic, transonic, and supersonic speed range. Three exchangeable test sections are designed with emphasis on different Mach number ranges. Regarding the coordinate system shown in Fig. 2, the inflow in the test section is along the x-axis. For the investigations presented in this paper, the closed transonic test section with perforated walls with a cross-section of $1.0m$ x $1.0m$ and a length of $4.5m$ was installed in the plenum chamber. The whole plenum chamber can be pressurized or evacuated, thus allowing to vary the total pressure and Reynolds number independently of the Mach number. The possible total pressure range in the plenum chamber is between $30kPa < p_{tot} < 150kPa$. The total temperature T_{tot} can be regulated between $293K < T_{tot} < 315K$. With this wind tunnel setup, a Mach number range of $0.30 < Ma_\infty < 1.20$ can be covered. Between $Ma_\infty = 0.90$ and $Ma_\infty = 1.20$, the wind tunnel flow needs additional suction through the perforated walls with a porosity of 6% to avoid a blockage effect due to the wall boundary layer. The turbulence level varies between 0.10% and 0.25%, depending on the flow conditions.

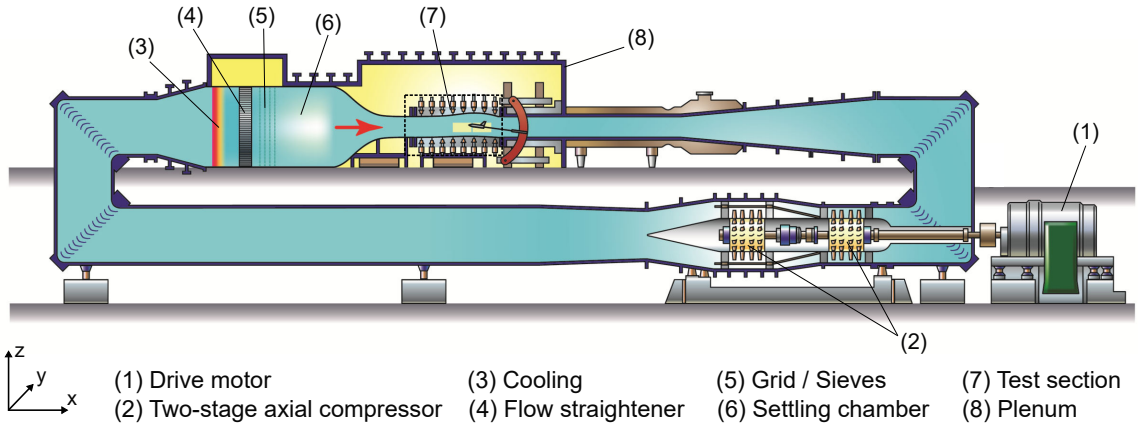

Figure 2 – Schematic illustration of the Transonic Wind Tunnel Göttingen (DNW-TWG)

3.2 Measurement Setup

A hydraulic pitch system actuates the DLR-F23 wind tunnel model in the test section of the Transonic Wind Tunnel. The half-span model with integrated peniche is installed on a turnable disk, as shown in Fig. 3. The motion from the rotational hydraulic cylinder, which is positioned outside the wind tunnel test section, is transmitted by a bellow coupling and a shaft. The actuation system is used to set a discrete angle of attack to perform steady polars. The angle of attack can be computed from the vertical distance measurement of two laser triangulators positioned upstream and downstream of the rotation axis below the model. Furthermore, a piezoelectric six-component balance is installed between the connecting plate of the wind tunnel model and the pitch actuator. A more detailed description of the design of the wind tunnel test section and the test rig used for the measurement campaign is given in Wiggen and Voß [19].

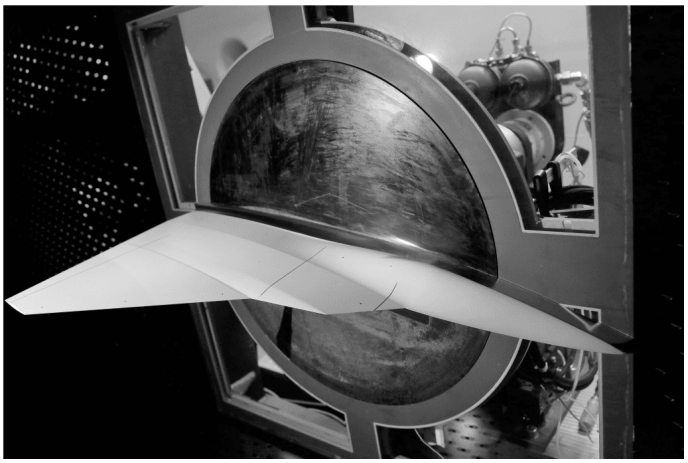

Figure 3 – DLR-F23 installed in the wind tunnel test section and coated with iPSP

3.3 Measurement Methods

This section describes the measurement methods used in the measurement campaign in detail. For the analysis of the unsteady surface pressures on the upper side of the DLR-F23 wind tunnel model, measurements with unsteady pressure transducers and with the iPSP method were conducted.

3.3.1 Fast-response Pressure-Sensitive Paint

Fast-response pressure-sensitive paint (iPSP) offers optical measurements of unsteady pressure changes on a surface with high spatial and temporal resolution. The iPSP measurement method is based on the photoluminescence of organic molecules in a polymer matrix and can be applied to complex surfaces such as the DLR-F23 configuration presented in this paper. The pressure-sensitive paint used in this work was developed by DLR and the University of Hohenheim based on the formulation by Gregory et al. [12] investigating high-frequency flow phenomena in aerodynamics. The paint is composed of a polymer/ceramic base layer and an active layer. The base layer consists of a mixture of a polymer (Duromax B-1000), ceramic particles (titanium silicon oxide $TiSiO_4$ with a particle size of 50 nm), a dispersant, and distilled water, see Gößling et al. [20]. The active layer includes toluene and PtTFPP as the luminophore (Pulkin et al. [21]). Further details of polymer/ceramic PSP are given in Liu et al. [22]. The paint was applied on-site to the surface of the model using a spray gun. A total paint layer thickness of 20 µm was achieved on the wind tunnel model. In order to measure the unsteady pressure distribution, the intensity method was used in this work. This method requires continuous excitation of the paint from the UV light. A high-speed CMOS camera measures the intensity of the light emission. The sensor equipment is located outside the closed test section on the optical windows of the side walls. The model is illuminated with five high-power LEDs, which emit light with a central wavelength of 490 nm. All LEDs have band-pass filters (385ET70) for wavelengths between 350 nm and 420 nm. The test setup uses one ultra-high-speed camera of type Photron Mini AX 200. The camera features a 12-bit CMOS sensor with a Canon 24 mm lens and a band-pass filter (ET650FS100) for wavelengths between 600 and 700 nm. The camera is configured to record images with a 1024 x 1024 pixels resolution. The camera image recording has a frame rate of 3200 Hz. The recorded images are finally mapped onto a 3D grid of the wind tunnel model.

3.3.2 Unsteady Pressure Transducers

In order to analyze the unsteady aerodynamics, the DLR-F23 is instrumented with 75 piezo-resistive surface pressure transducers (Kulite XCQ-132A-093) on the upper side of the wing. The unsteady pressure transducers are arranged in three spanwise aligned pressure sections shown in Fig. 1. The first section S_1 with 12 pressure transducers is located at the LEVCON at $x/c_{r,W} = 0.557$ from the origin of the body-fixed coordinate system. The second section S_2 with 33 transducers is positioned at the strake at $x/c_{r,W} = 0.835$. The transducers in the first and second rows have an equidistant spacing in the spanwise direction of $y = 5\,mm$. The pressure section S_4 with 30 transducers at the

main wing ($x/c_{r,W} = 1.357$) has an equidistant spacing of $y = 10\,mm$. The data acquisition of the pressure transducers is synchronized, and the sampling frequency range is between $f_s = 0.5\,kHz$ and $f_{s,max} = 29.2\,kHz$. Concerning the frequency of the respective unsteady flow phenomena to be analyzed, a ten times higher sampling frequency was considered. In addition, pressure ports with a sampling frequency of $f_s = 200\,Hz$ are installed at the wind tunnel walls.

3.4 Measurement Conditions

The measurements were performed in a Mach number range between $Ma_\infty = 0.55$ and $Ma_\infty = 1.15$ with a Mach number interval of 0.1. The Reynolds number related to the mean aerodynamic chord is in the range of $2.35 \times 10^6 < Re_{l_\mu} < 3.27 \times 10^6$. The measurements were conducted in an AoA range from $\alpha = 0°$ to $\alpha = 30°$ in the Mach number range from $Ma_\infty = 0.55$ to $Ma_\infty = 0.85$. Due to the increase in aerodynamic loads, the maximum AoA was reduced in the higher Mach number range. The maximum possible wind tunnel blockage of 10% is reached at an AOA of $\alpha = 32.7°$ for the presented model setup. The measurement conditions for the experimental investigations at the Transonic Wind Tunnel Göttingen are shown in Table 2.

Table 2 – Measurement conditions

Parameter	**Value**
Mach number Ma_∞	0.55 - 1.15
Reynolds number $Re_{l_\mu} = (\rho_\infty U_\infty l_\mu)/\mu$	2.35×10^6 - 3.26×10^6
Angle of attack α	0° - 30° ($0.55 \leq Ma_\infty \leq 0.85$) 0° - 25° ($Ma_\infty = 0.95$) 0° - 20° ($Ma_\infty \geq 1.05$)

4. Results and Discussion

This chapter describes the analysis and interpretation of the experimental results of the pressure-sensitive paint measurements on the DLR-F23 half-span wind tunnel model. The paper focuses on three selected flow conditions in the subsonic, transonic, and supersonic speed range. The evaluation concentrates on the analysis of the surface pressure distributions, the surface traces of the vortex trajectories, and the evaluation of the pressure distributions along the vortex trajectories on the surface of the upper side of the wing. The vortex-dominated aerodynamics of the triple-delta-wing configuration is analyzed considering complex phenomena such as vortex-vortex interactions, vortex-shock interactions, and vortex breakdown.

4.1 Subsonic Flow Condition

The investigated subsonic flow condition is defined by a Mach number of $Ma_\infty = 0.65$ and a Reynolds number of $Re_{l_\mu} = 2.62 \times 10^6$ at an angle of attack of $\alpha = 18°$. As described in Section 1, multiple leading-edge vortices develop on hybrid-delta wings with multiple swept leading edges. In particular, three discrete leading-edge vortices can be identified on the DLR-F23 configuration under subsonic flow conditions. The mean pressure distribution $\bar{c}_p$ in Fig. 4a shows clearly the vortex trajectories as surface traces or 'footprints', charaterized by negative pressure peaks. Figure 4b shows the pressure fluctuations $c_{p,rms}$, which is a measure of the fluctuations in surface pressure. At the cosine-chined forebody, which is not in the resolved iPSP measurement zone, the so-called inboard vortex (IBV) develops. The IBV can also be described as the forebody vortex. The separated shear layer on the LEVCON generates another leading-edge vortex, which is defined as the midboard vortex (MBV). At the strake, no independent vortex is formed. Instead, the separated shear layer interacts directly with the separated shear layer of the LEVCON and forms a combined vortex. For this reason, the MBV can also be defined as the strake vortex. The so-called outboard vortex (OBV), also described as the main wing vortex, is formed at the kink between the strake and the main wing. The oscillations of the surface traces of the vortex trajectories can be detected in the pressure fluctuations in Fig. 4b.

Figure 5 shows the local Mach number distribution on the wing. The local Mach number is calculated using the isentropic flow equations according to Equation 1. The local static surface pressure is denoted as p and the total pressure as p_{tot}. A constant value of $\kappa = 1.4$ was used for the isentropic exponent.

$$Ma = \sqrt{\frac{2}{\kappa - 1}\left[\left(\frac{p}{p_{tot}}\right)^{\frac{1-\kappa}{\kappa}} - 1\right]} \tag{1}$$

Leading edge vortices are characterized by high axial accelerations along the axis of rotation, which results in overspeeds in the vortex core. According to the literature, the mean axial velocity component in a leading-edge vortex core is 2 to 5 times the flow velocity [23]. In the region of the vortex trajectory of the MBV at the LEVCON, maximum local Mach numbers of $Ma = 1.80$ are reached as a result of the overspeeds in the vortex core. This maximum local Mach number corresponds to 2.8 times the inflow Mach number.

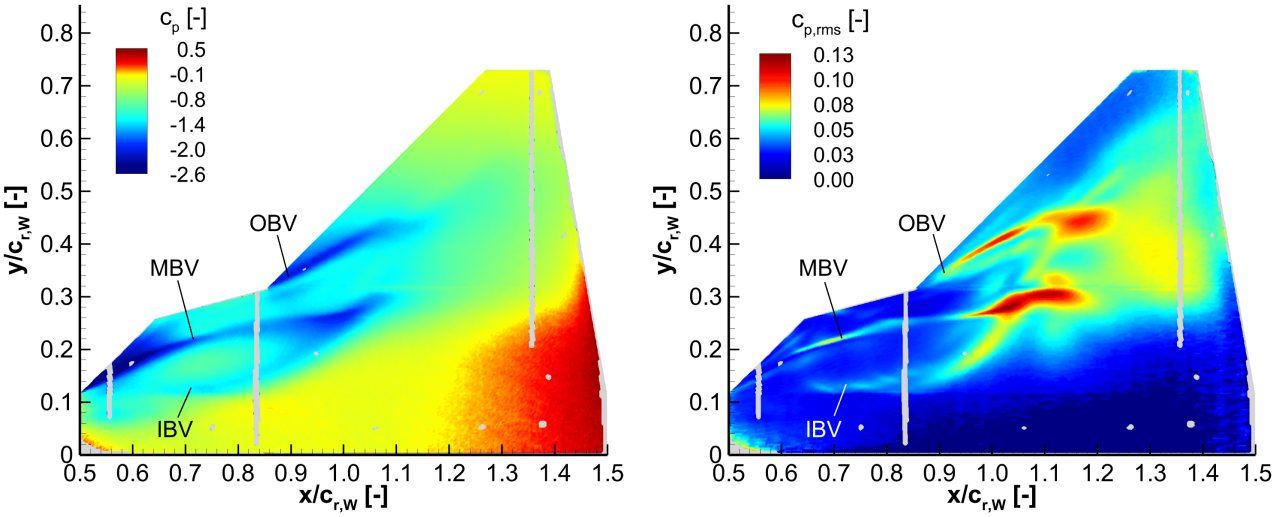

(a) Mean pressure distribution $\bar{c}_p$

(b) Pressure fluctuations $c_{p,rms}$

Figure 4 – Surface pressure distribution for $Ma_\infty = 0.65$ and $Re_{l_\mu} = 2.62 \times 10^6$ at $\alpha = 18°$

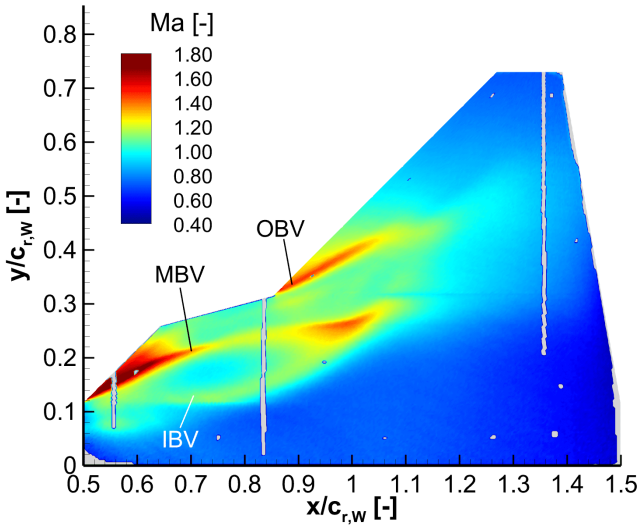

Figure 5 – Local Mach number distribution for $Ma_\infty = 0.65$ and $Re_{l_\mu} = 2.62 \times 10^6$ at $\alpha = 18°$

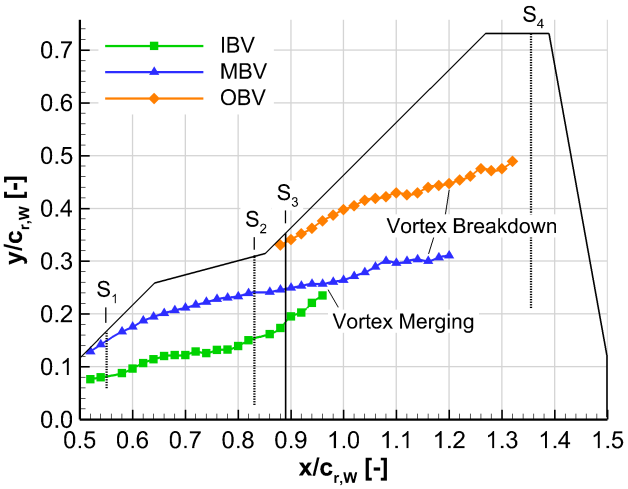

(a) Surface traces of the vortex trajectories

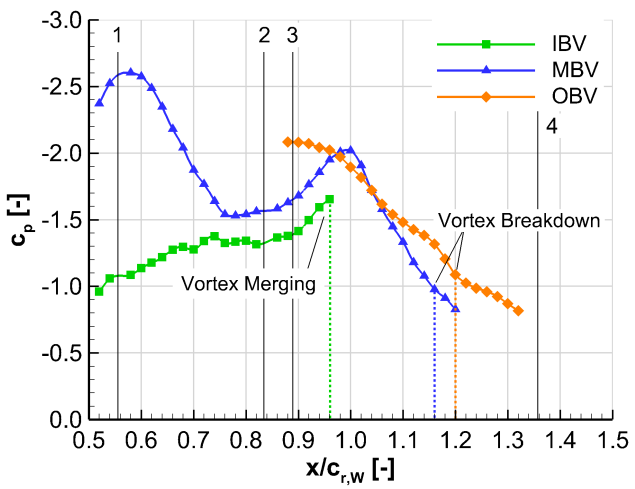

(b) Pressure distribution along the vortex trajectories

Figure 6 – Surface traces of the vortex trajectories for $Ma_\infty = 0.65$ and $Re_{l_\mu} = 2.62 \times 10^6$ at $\alpha = 18^\circ$

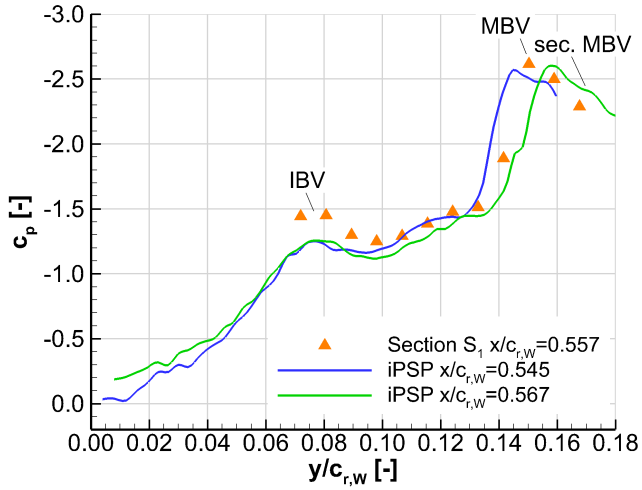

(a) Pressure section S_1 $(x/c_{r,W} = 0.557)$

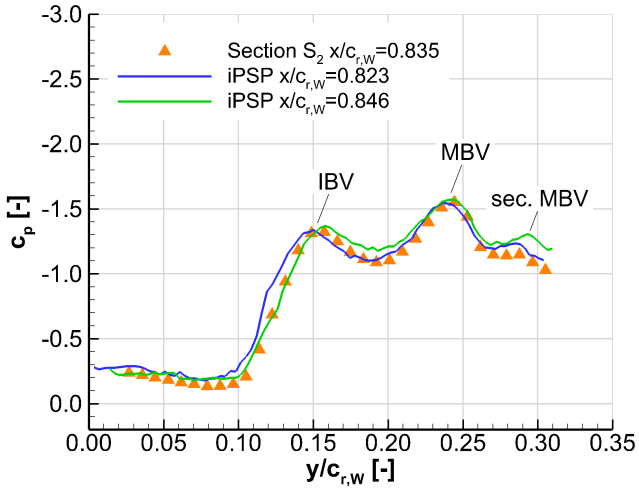

(b) Pressure section S_2 $(x/c_{r,W} = 0.835)$

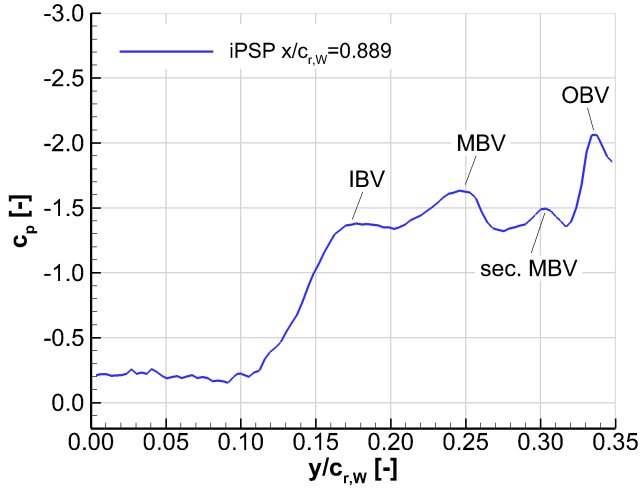

(c) Pressure section S_3 $(x/c_{r,W} = 0.889)$

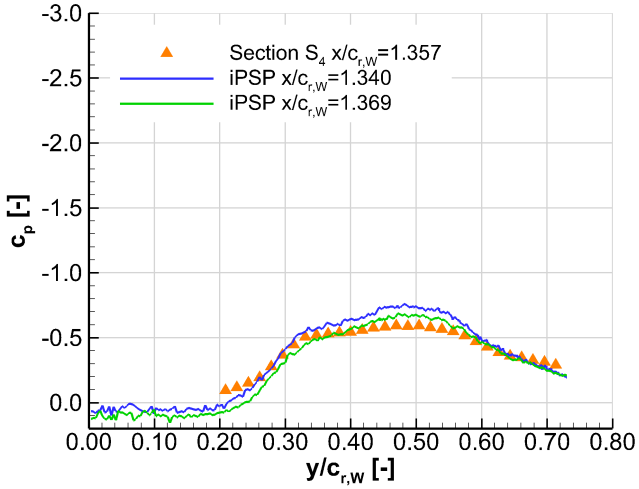

(d) Pressure section S_4 $(x/c_{r,W} = 1.357)$

Figure 7 – Surface pressure sections for $Ma_\infty = 0.65$ and $Re_{l_\mu} = 2.62 \times 10^6$ at $\alpha = 18^\circ$

Figure 6a shows the surface traces of the vortex trajectories of the IBV, MBV, and OBV on the upper side of the wing. Figure 6b shows the corresponding surface pressure distribution along the vortex

trajectories. The position of the surface traces is identified by evaluating the surface pressure sections in the spanwise direction. The suction peak, which corresponds to the local pressure minimum, of the specific vortex is determined. Figure 7 compares the surface pressure sections of the iPSP data of four selected positions ($x/c_{r,W} = 0.557, 0.835, 0.889, 1.357$) with the spanwise aligned pressure sections of the unsteady pressure transducers. The ports of the pressure transducers have to be taped for the iPSP measurements. For this reason, no iPSP data is available for the pressure sections. The pressure sections of the unsteady pressure transducers are compared with two iPSP pressure sections, one positioned upstream and one downstream.
In pressure section S_1 ($x/c_{r,W} = 0.557$), shown in Fig. 7a, the suction peak of the IBV is located at $y/c_{r,W} = 0.080$. Compared with the pressure measurements, the suction peak for the iPSP pressure sections is 15% lower, but the spanwise position is the equivalent. The suction peak of the MBV is located at $y/c_{r,W} = 0.150$ and reaches $c_p = -2.575$. The local minima of the MBV of the iPSP sections are shifted due to the short distance in the chordwise direction. In pressure section 1, the MBV is significantly stronger than the IBV, according to Fig. 6b. In comparison to the suction peak of the IBV, the MBV has a negative pressure that is 2.2 times lower. The side peak in the region of the MBV in the iPSP pressure sections, shown in Fig. 7a, can be assigned to the secondary vortex of the MBV. The suction peak of the secondary vortex cannot be identified in the pressure section of the pressure transducers due to the limited equidistant spacing between the pressure ports. In pressure Section S_2, according to Fig. 7b, the IBV is located at $y/c_{r,W} = 0.150$ and the MBV at $y/c_{r,W} = 0.245$. In comparison to pressure section S_1, the pressure minimum of the suction tip of the MBV is reduced by 41%. In pressure section S_2, the secondary vortex of the MBV at $y/c_{r,W} = 0.290$ is considerably more developed than in section S_1. The comparison between the pressure data of the unsteady pressure transducers and the iPSP measurement shows a good correlation over the entire spanwise distribution. In Figure 6a, the surface traces of the IBV and the MBV show that the vortex core of the IBV is moving to the MBV. Figure 7c presents the pressure section S_3 at $x/c_{r,W} = 0.889$, which analyzes the spanwise pressure distribution of the first part of the main wing. There is no pressure section of the unsteady pressure transducers at this chordwise position; therefore, only the iPSP data is shown. The suction peak of the IBV has shifted further towards the MBV compared to pressure section S_2. The suction peak of the OBV, which develops at the leading edge of the main wing, is located at $y/c_{r,W} = 0.335$. The pronounced pressure minimum of the OBV is 28% lower compared to the MBV.

In Fig. 6a, a vortex merging between the IBV and the MBV can be observed at $x/c_{r,W} = 0.960$. In the region of $x/c_{r,W} = 0.80$ it can be seen that due to the mutual influence of the two vortices, the surface trace of the IBV moves outwards, and the MBV shifts slightly inboard. The shifting of the weaker IBV towards the MBV increases due to the stronger MBV, and finally, the IBV merges into the MBV. According to the literature, merged vortices are more stable and produce a stronger low-pressure field, which increases the overall lift of the wing [24]. The primary mechanism of vortex merging involves the exchange of momentum and energy, which can result in the vortices combining into a single, larger vortex. This can be observed in the present vortex merging in Fig. 6b in a strong increase in the negative pressure of the combined IBV vortex after the merging process at $x/c_{r,W} = 1.00$. The analysis of the pressure distribution along the vortex trajectories in Fig. 6b shows the position of the vortex breakdown of the MBV and the OBV based on the evaluation of the iPSP data. The position of vortex breakdown is identified, as the vortex breakdown is correlated to a strong pressure increase. In addition, the spanwise pressure sections in the region of the vortex breakdown locations are analyzed with regard to the suction peaks. The vortex breakdown position of the MBV is at $x/c_{r,W} = 1.16$ and that of the OBV at $x/c_{r,W} = 1.20$. In Fig. 7d for pressure section S_4 ($x/c_{r,W} = 1.357$), the turbulent wake of the burst vortices can be identified. The turbulent wake has a broad-band shape starting from $y/c_{r,W} = 0.20$ up to the wing tip.

4.2 Transonic Flow Condition

At a Mach number of 0.85 and an angle of attack of $\alpha = 21°$, the previously mentioned unsteady flow phenomena such as vortex-vortex interactions, vortex-shock interactions and vortex breakdown can be observed. Figure 8a shows the mean values of the pressure coefficient $\overline{c}_p$ on the upper side of the wing. Figure 8b shows the root mean square values $c_{p,rms}$ of the pressure coefficient. The

analyzed vortex system for the transonic flow conditions consists of three leading-edge vortices, as for the previously discussed subsonic case for $Ma_\infty = 0.65$. Figure 9 shows the local Mach number distribution on the wing. The local Mach number is calculated according to Equation 1. In the region of the vortex trajectory of the MBV at the LEVCON, maximum local Mach numbers of $Ma = 2.40$ can be observed due to the overspeeds in the vortex core. The iPSP data can also be used to identify the position and oscillation of the shocks that occur due to the transonic flow conditions. The position of the first normal shock at $x/c_{r,W} = 0.725$ can be determined by a steep gradient in the pressure coefficient in Fig. 8a. In the evaluation of the pressure fluctuations according to Fig. 8b, it can be seen that the first shock oscillates in its position. In the area between $x/c_{r,W} = 0.980$ and $x/c_{r,W} = 1.020$, the formation of a second normal shock can be observed. The exact position of the second shock cannot be precisely determined from the iPSP surface pressure data, since several unsteady flow phenomena are superimposed in this area.

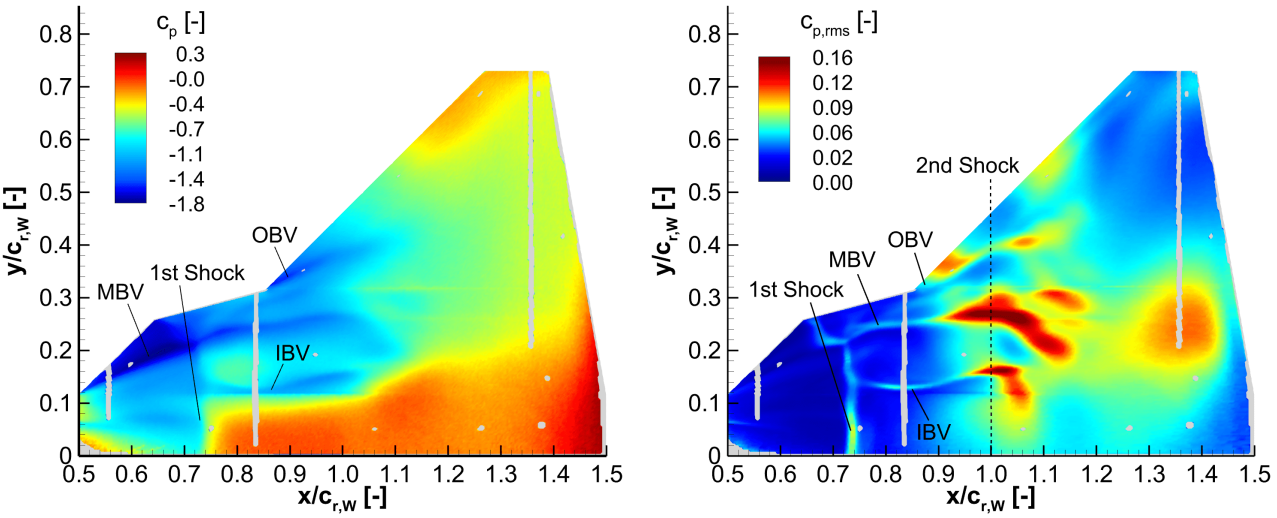

(a) Mean pressure distribution $\bar{c}_p$

(b) Pressure fluctuations $c_{p,rms}$

Figure 8 – Surface pressure distribution for $Ma_\infty = 0.85$ and $Re_{l_\mu} = 3.02 \times 10^6$ at $\alpha = 21°$

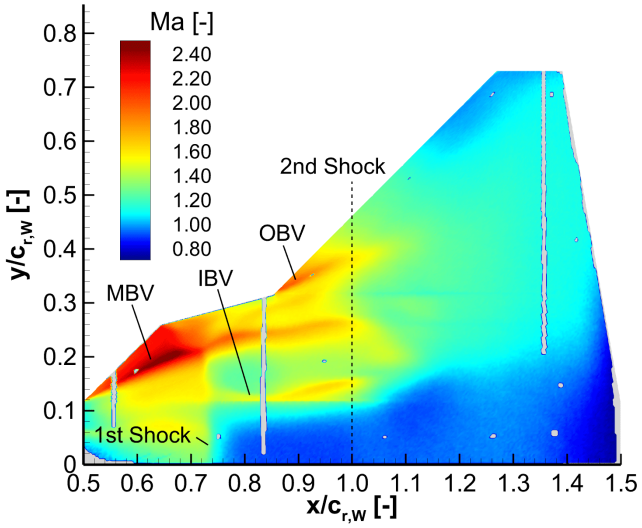

Figure 9 – Local Mach number distribution for $Ma_\infty = 0.85$ and $Re_{l_\mu} = 3.02 \times 10^6$ at $\alpha = 21°$

Figure 10 shows the surface traces of the vortex trajectories of the IBV, MBV, and OBV. Figure 11 compares the surface pressure sections of the iPSP data of four selected positions ($x/c_{r,W} = 0.557, 0.835, 0.889, 1.357$) with the pressure sections of the unsteady pressure transducers. In pressure section S_1 ($x/c_{r,W} = 0.557$), shown in Fig. 11a, the suction peak of the IBV is located at $y/c_{r,W} = 0.056$.

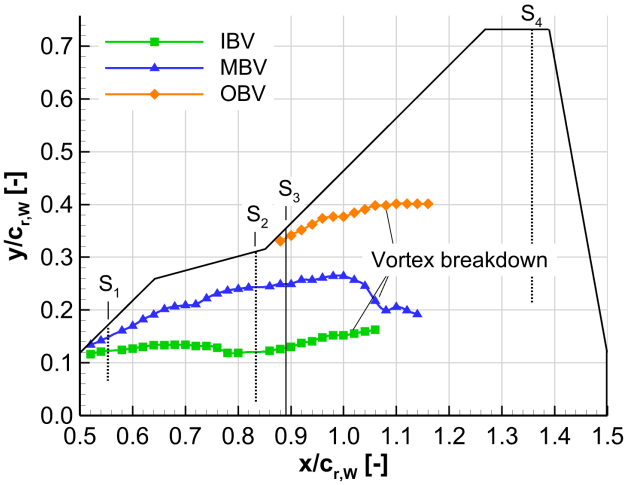

(a) Surface traces of the vortex trajectories

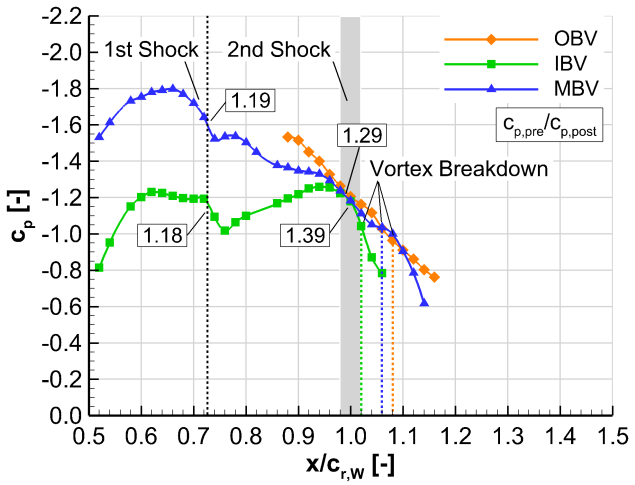

(b) Pressure distribution along the vortex trajectories

Figure 10 – Surface traces of the vortex trajectories for $Ma_\infty = 0.85$ and $Re_{l_\mu} = 3.02 \times 10^6$ at $\alpha = 21^\circ$

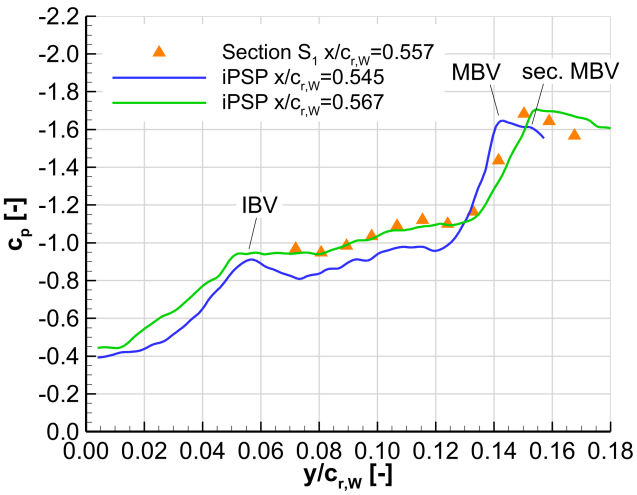

(a) Pressure section S_1 $(x/c_{r,W} = 0.557)$

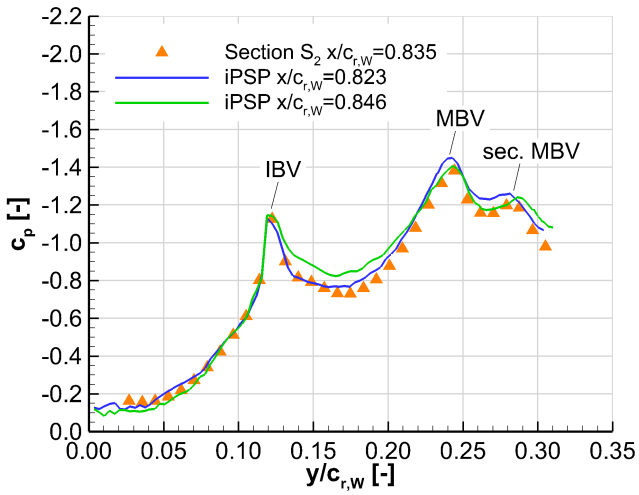

(b) Pressure section S_2 $(x/c_{r,W} = 0.835)$

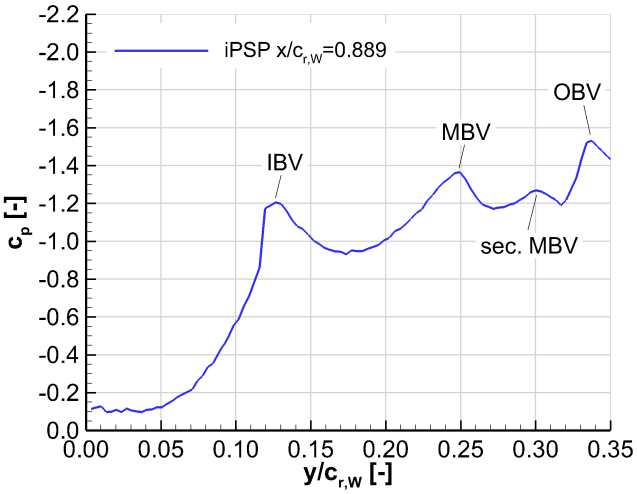

(c) Pressure section S_3 $(x/c_{r,W} = 0.889)$

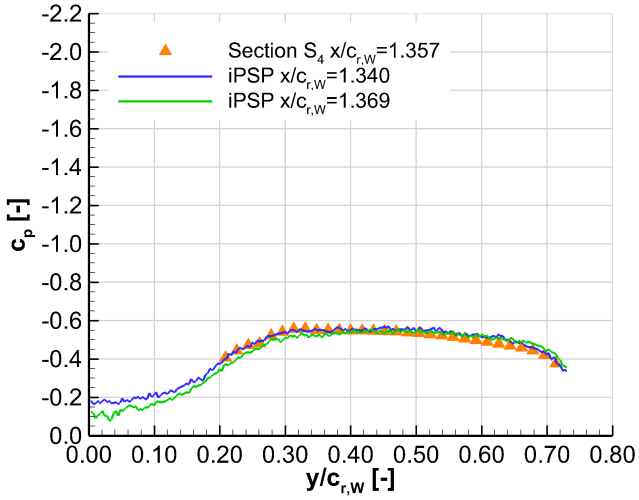

(d) Pressure section S_4 $(x/c_{r,W} = 1.357)$

Figure 11 – Surface pressure sections for $Ma_\infty = 0.85$ and $Re_{l_\mu} = 3.02 \times 10^6$ at $\alpha = 21^\circ$

The suction peak of the MBV is located at $y/c_{r,W} = 0.150$. In pressure section S_1, the MBV is significantly stronger than the IBV, with a 1.8 times higher suction peak. The pressure data from the un-

steady pressure transducers correlates with the iPSP pressure section for $x/c_{r,W} = 0.567$. In pressure section S_2, according to Fig. 11b, the IBV is located at $y/c_{r,W} = 0.122$ and the MBV at $y/c_{r,W} = 0.244$. In comparison to pressure section S_1, the suction peak of the IBV increases by 18%. The suction peak of the MBV has decreased by 20%. The decrease in the negative pressure of the suction peak of the MBV can be explained by the interaction with the first shock, which occurs at $x/c_{r,W} = 0.725$, as shown in Fig. 10b. The secondary vortex of the MBV is located at $y/c_{r,W} = 0.285$. The pressure data from the transient pressure transducers and the iPSP measurement have a high degree of correlation over the entire spanwise distribution. The secondary vortex of the MBV can also be identified in the pressure section of the unsteady pressure transducers. Figure 11c shows the iPSP pressure section S_3 at $x/c_{r,W} = 0.889$. There is no pressure section of the transient pressure transducers at this chordwise position; therefore, only the iPSP data is shown. The vortex suction peak of the IBV has not shifted its spanwise position, and the suction pressure level is slightly higher compared to pressure section S_2. The position of the suction peak of the MBV has shifted slightly in the direction of the wing tip compared to pressure section S_2 and is located at $y/c_{r,W} = 0.248$. The position of the suction peak of the MBV secondary vortex has moved further in the direction of the OBV to $y/c_{r,W} = 0.300$ compared to the pressure section S_2. The suction peak of the OBV, which develops at the leading edge of the main wing, is located at $y/c_{r,W} = 0.337$. The pronounced pressure minimum of the suction peak of the OBV is 13% higher compared to the MBV. In Fig. 11d for pressure section S_4 ($x/c_{r,W} = 1.357$), the turbulent wake of the burst vortices can be identified. The turbulent wake has a broad-band shape starting from $y/c_{r,W} = 0.10$ up to the wing tip.

In the pressure distribution along the vortex trajectories shown in Fig. 10b, starting from $x/c_{r,W} = 0.500$, an increase in negative pressure can be seen for both the IBV and the MBV. This indicates that the axial velocity component in the vortex cores is accelerating in this section. In the evaluation of the local Mach number according to Fig. 9, a significant overspeed in the trajectory of the MBV in the section between $x/c_{r,W} = 0.500$ and $x/c_{r,W} = 0.720$ can also be observed. The pressure distribution of the MBV has a global minimum at $x/c_{r,W} = 0.660$. In comparison, the pressure distribution of the IBV shows an approximately constant pressure from $x/c_{r,W} = 0.600$ up to the position of the first normal shock at $x/c_{r,W} = 0.725$. The pressure ratios $c_{p,pre}/c_{p,post}$ of the first normal shock are 1.18 for the IBV and 1.19 for the MBV. The primary vortices recover after passing the first normal shock. It can, therefore, be assumed that these are weak vortex-shock interactions according to the investigations of Schiavetta et al. [4]. In the pressure distribution of the MBV, a local pressure minimum at $x/c_{r,W} = 0.780$ can be observed after the first normal shock. A continuous increase in pressure can be identified in the further pressure distribution. In comparison, a decrease in pressure can be observed in the pressure distribution of the IBV up to a local pressure minimum at $x/c_{r,W} = 0.942$.
In the section of the second normal shock between $x/c_{r,W} = 0.980$ and $x/c_{r,W} = 1.020$, high adverse pressure gradients occur along the surface traces of the IBV and MBV. The pressure ratios $c_{p,pre}/c_{p,post}$ of the second normal shock are 1.39 for the IBV and 1.29 for the MBV. In comparison to the IBV and MBV, no significant adverse pressure gradient can be observed in the pressure distribution of the OBV in the area of the second normal shock. Instead, a continuous increase in pressure can be identified over the entire pressure distribution of the OBV. The vortex-shock interaction for the second normal shock can be interpreted as a strong interaction according to Delery [25] and causes a considerable weakening of the vortex core for both the IBV and the MBV. The vortex breakdown position of the IBV is at $x/c_{r,W} = 1.02$ and that of the MBV at $x/c_{r,W} = 1.06$. Due to the strong interaction between the second normal shock and the IBV and MBV, vortex bursting can be characterized as shock-induced vortex breakdown. The identified vortex breakdown position of the OBV is at $x/c_{r,W} = 1.08$. Based on the pressure distribution of the surface trace of the vortex and the bursting position further downstream, a weak interaction is assumed for the OBV.

In order to gain an in-depth understanding of the unsteady surface pressure distribution of the iPSP measurements, the Proper Orthogonal Decomposition (POD) was used. The POD method extracts important flow features and patterns as a compact representation of the highly dimensional fluid data [18]. POD represents a decomposition of the data into a series of orthogonal modes based on the spatio-temporal correlation of the original data. The POD modes are ordered according to the energy

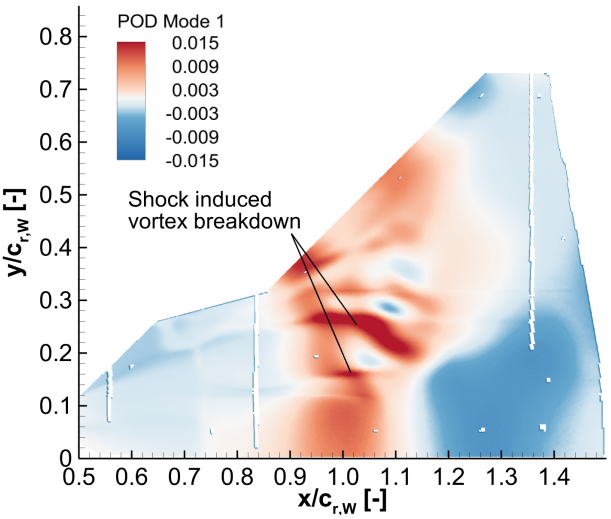

(a) POD Mode 1

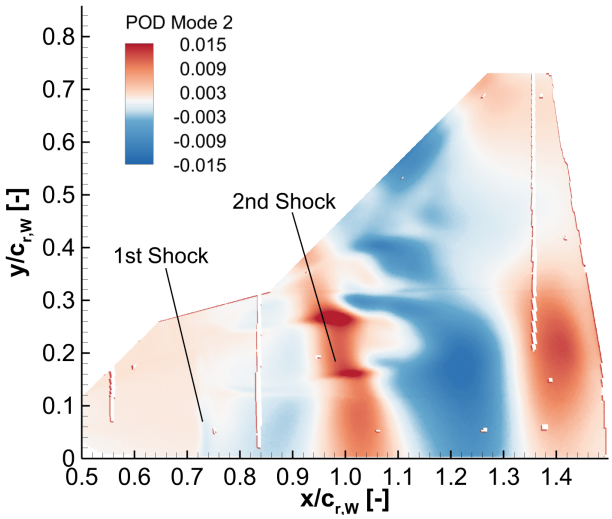

(b) POD Mode 2

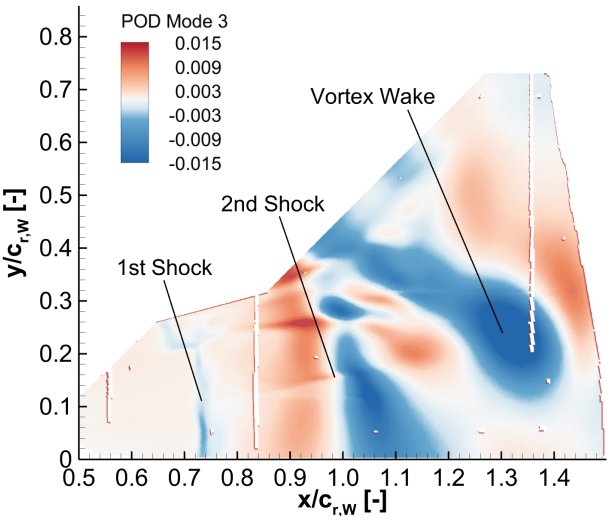

(c) POD Mode 3

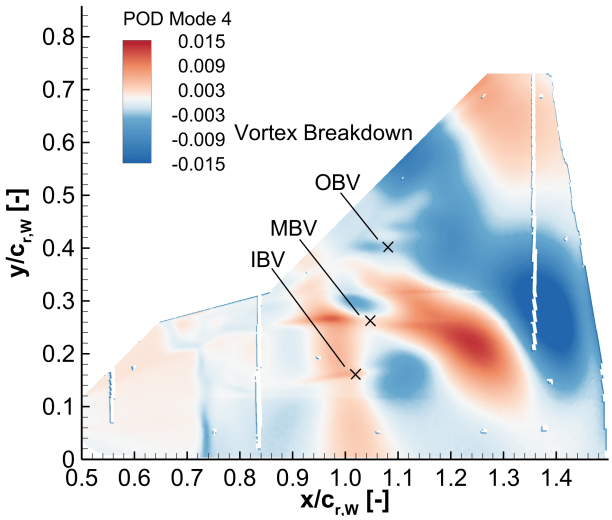

(d) POD Mode 4

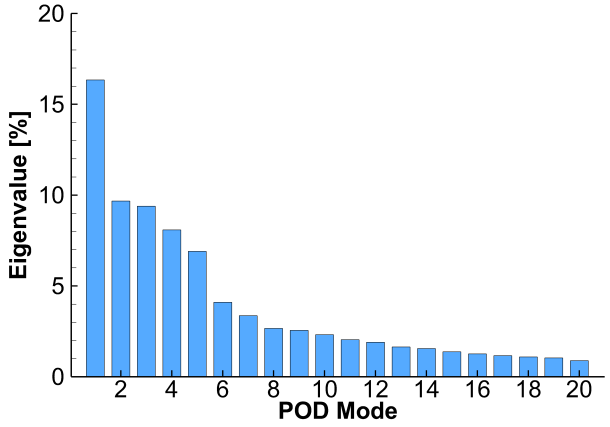

(e) Eigenvalues of modes 1 to 20

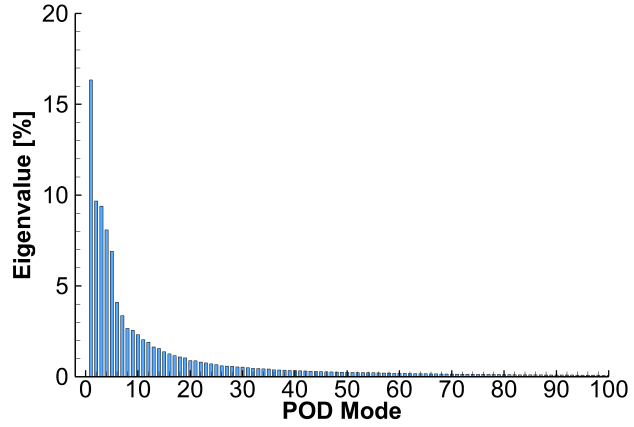

(f) Eigenvalues of modes 1 to 100

Figure 12 – POD analysis for $Ma_\infty = 0.85$ and $Re_{l_\mu} = 3.02 \times 10^6$ at $\alpha = 21^\circ$

they contain in the original data. Figure 12 shows the POD results for the high-energy modes, mode 1 to mode 4, based on iPSP data for the transonic flow condition at $Ma_\infty = 0.85$. Figures 12e and 12f show the eigenvalues of the modes, which correlate with the energy level of the respective modes. According to Fig. 12e, the energy content of the first five POD modes is more than 50%. The first 20 modes represent more than 80% of the total energy content in the POD evaluation. The POD

mode 1 in Fig. 12a represents the shock-induced vortex breakdown of the IBV and the MBV in the region of the main wing. Based on the eigenvalue analysis, this mode has the highest energy content in the unsteady flow field. The alternating areas of negative and positive amplitudes represent the high levels of fluctuations caused in the vortex breakdown area. In the evaluation of the POD mode 2 in Fig.12b, the unsteady characteristics of the position of the second normal shock in the section between $x/c_{r,W} = 0.980$ and $x/c_{r,W} = 1.020$ can be observed. The fluctuations of the bursting vortex cores of the IBV and the MBV are superimposed with the mode of the second shock. The evaluation of the POD mode 3 shows the first normal shock at $x/c_{r,W} = 0.725$ according to Fig. 12c. The first shock is developed starting from the leading edge in the area of the kink between the LEVCON and the strake. In the section of the main wing, the area of the burst vortex wake can be identified. The analysis of the POD mode 4 in Fig. 12d shows the vortex breakdown positions of the three primary vortices.

4.3 Supersonic Flow Condition

The supersonic flow condition discussed in this section is defined by a Mach number of $Ma_\infty = 1.15$ and a Reynolds number of $Re_{l_\mu} = 3.27 \times 10^6$ at an angle of attack of $\alpha = 12°$. For this case, the compressible flow phenomena and the vortex-shock interactions are the main focus of the analysis. The mean pressure distribution in Fig. 13a shows the surface trace of the IBV vortex trajectory at a spanwise position of $y/c_{r,W} = 0.120$. The surface trace of the IBV can also be observed in the pressure fluctuations according to Fig. 13b. The vortex trajectory of the MBV can be observed in the section of the main wing both in the mean pressure distribution and the pressure fluctuations. Compared to the transonic flow condition for $Ma_\infty = 0.85$, a partially developed OBV in the section of the main wing is generated for the supersonic case. Generally, it can be observed that due to the reduced magnitude of the suction peaks, the footprint of the vortices becomes less clear, and, therefore, the trajectory of the vortices becomes more and more indistinct at higher Mach numbers.

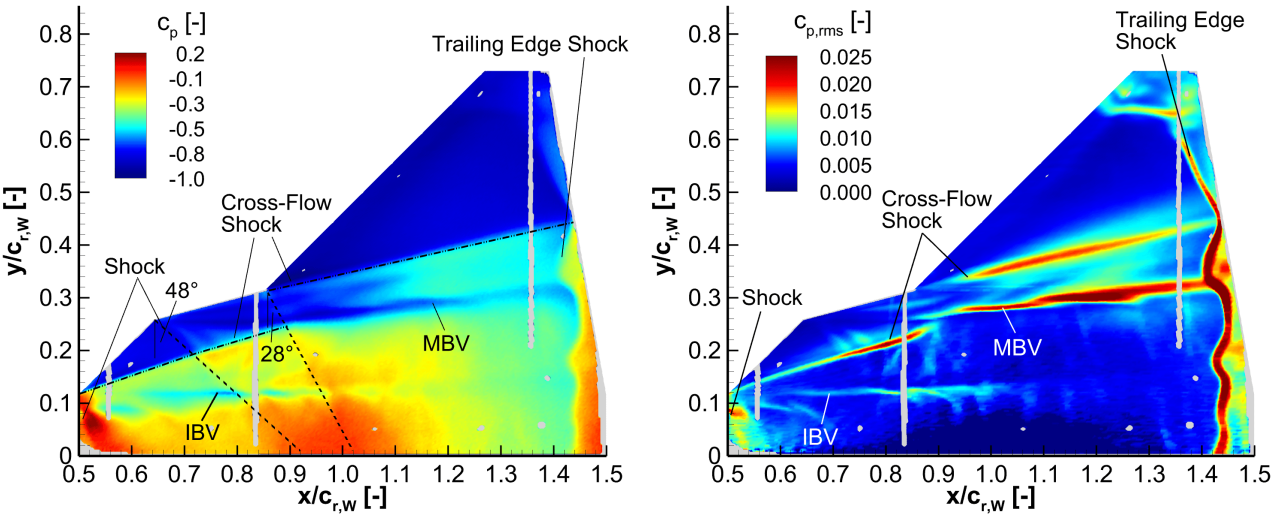

(a) Mean pressure distribution $\bar{c}_p$

(b) Pressure fluctuations $c_{p,rms}$

Figure 13 – Surface pressure distribution for $Ma_\infty = 1.15$ and $Re_{l_\mu} = 3.27 \times 10^6$ at $\alpha = 12°$

For supersonic speeds, it is decisive whether the component of the Mach number perpendicular to the leading edge of the wing, $Ma_{\infty,n}$, is lower or higher than $Ma_{\infty,n} = 1$. A subsonic leading edge is defined by a Mach number $Ma_{\infty,n} < 1$ and is characterized by a complete flow around the leading edge. When the Mach number reaches the value of $Ma_{\infty,n} = 1$, this is referred to as a sonic leading edge. In the case of a supersonic leading edge at $Ma_{\infty,n} > 1$, there is no flow around the leading edge. According to Stanbrook and Squire [26], the component $Ma_{\infty,n}$, as defined by Eq. 2, depends not only on the wing sweep φ and free stream Mach number Ma_∞ but also on the angle of attack α.

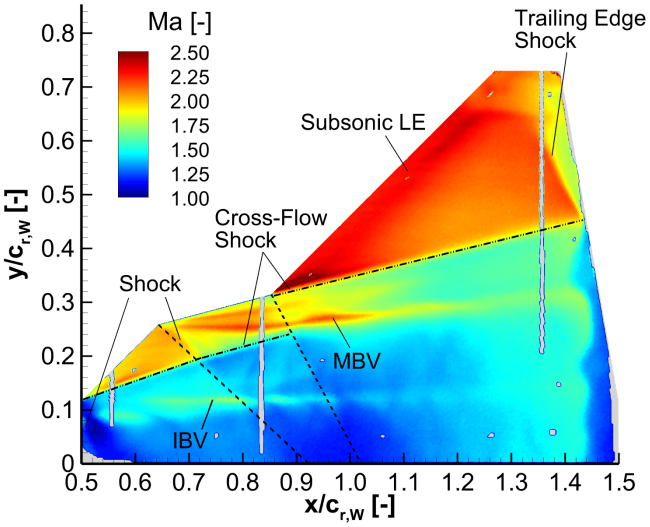

Figure 14 – Local Mach number distribution for $Ma_\infty = 1.15$ and $Re_{l_\mu} = 3.27 \times 10^6$ at $\alpha = 12°$

$$Ma_{\infty,n} = Ma_\infty \cdot cos(\varphi)[1 + sin^2(\alpha) \cdot tan^2(\varphi)]^{\frac{1}{2}} \quad \begin{cases} < 1 & \text{Subsonic leading edge} \\ = 1 & \text{Sonic leading edge} \\ > 1 & \text{Supersonic leading edge} \end{cases} \tag{2}$$

For the present supersonic case, a normal Mach number of $Ma_{\infty,n} = 0.83$ can be derived from Eq. 2 for the leading edge of the LEVCON. The normal Mach number for the strake is $Ma_{\infty,n} = 0.38$, and the normal Mach number for the main wing is equal to that for the LEVCON due to the same leading-edge sweep. Therefore, only subsonic leading edges are present. The normal Mach number values from Eq. 2 are theoretical limits. It is assumed that a bow shock forms at the nose of the DLR-F23 wind tunnel model for this flow case, similar to the experimental investigations for the DLR-F22 configuration [27]. This bow shock causes a change in the free stream conditions for the subsequent leading edges.

In Fig. 13a, an attached normal shock can be identified in the transition between the forebody and the LEVCON at $x/c_{r,W} = 0.510$. A second normal shock starts from the leading edge at the transition between LEVCON and Strake at $x/c_{r,W} = 0.655$. This second shock propagates at an angle of 48° to the y-axis in the direction of the inboard area and interacts with the MBV at $x/c_{r,W} = 0.705$ and with the IBV at $x/c_{r,W} = 0.805$. A third normal shock is identified at the kink of the main wing, which propagates at an angle of 28° to the y-axis in the direction of the inboard area, similar to the second shock. A vortex-shock interaction with the third shock can be observed with the MBV at $x/c_{r,W} = 0.885$ and with the IBV at $x/c_{r,W} = 0.958$.
In Fig. 13a, a cross-flow shock in the direction of the vortex core of the MBV can be identified in the mean pressure distribution. According to Squire [28], and Elsenaar et al. [29], these shocks are located along the primary vortex for transonic and supersonic flow conditions. The shock wave of the cross-flow shock can be located under the primary vortex or above the primary vortex [30]. The shock wave under the primary vortex is caused by the fact that supersonic cross-flow under the primary vortex is decelerated toward the secondary separation by passing through a locally normal shock. In the local Mach number distribution, shown in Fig. 14, the first cross-flow shock develops along the trajectory of the MBV and interacts with the normal shock at $x/c_{r,W} = 0.715$ and with the second normal shock at $x/c_{r,W} = 0.890$. The vortex-shock interaction leads to a weakening of the MBV and, therefore, a weakening of the associated cross-flow shock. A second cross-flow shock, shown in Fig. 14, forms at the kink to the main wing and develops along the OBV. As already stated, the OBV is only partially developed for this supersonic flow condition.

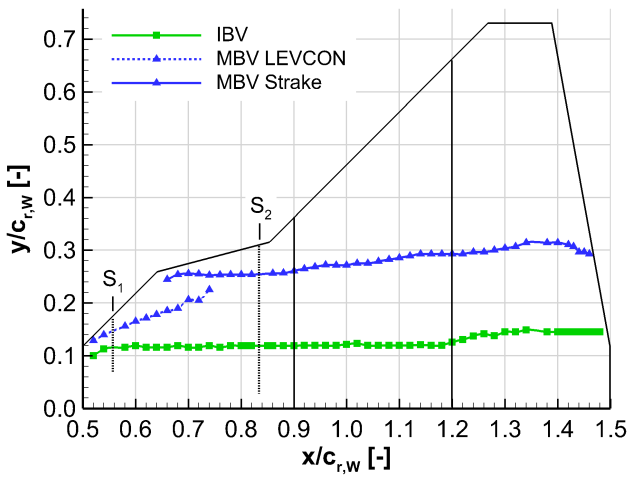

(a) Surface traces of the vortex trajectories

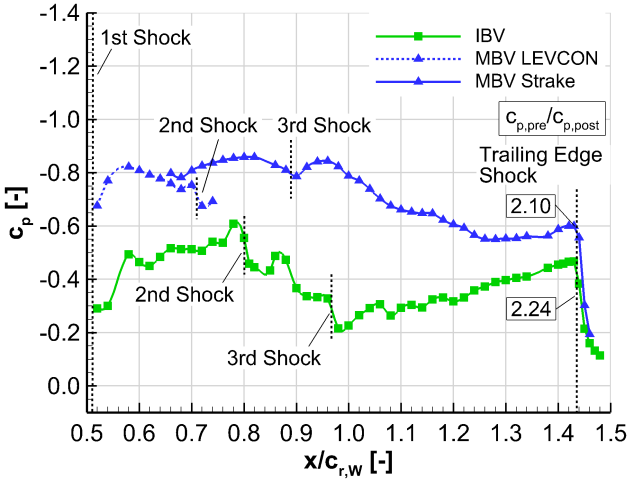

(b) Pressure distribution along the vortex trajectories

Figure 15 – Surface traces of the vortex trajectories for $Ma_\infty = 1.15$ and $Re_{l_\mu} = 3.27 \times 10^6$ at $\alpha = 12^\circ$

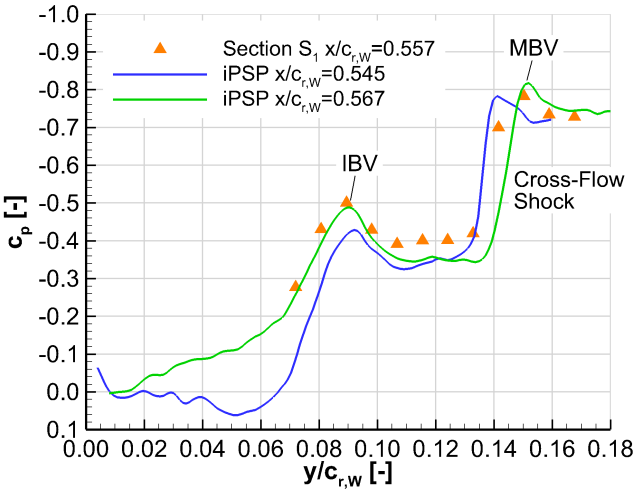

(a) Pressure section S_1 $(x/c_{r,W} = 0.557)$

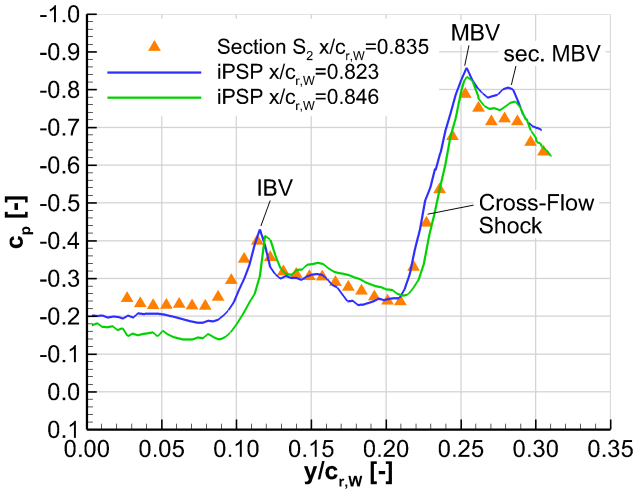

(b) Pressure section S_2 $(x/c_{r,W} = 0.835)$

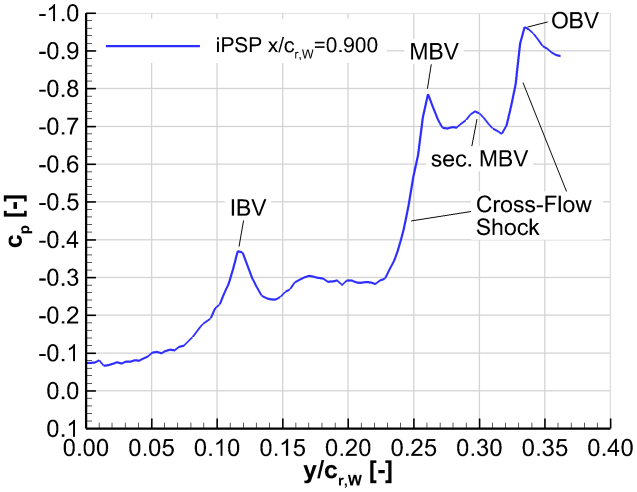

(c) Pressure section $x/c_{r,W} = 0.900$

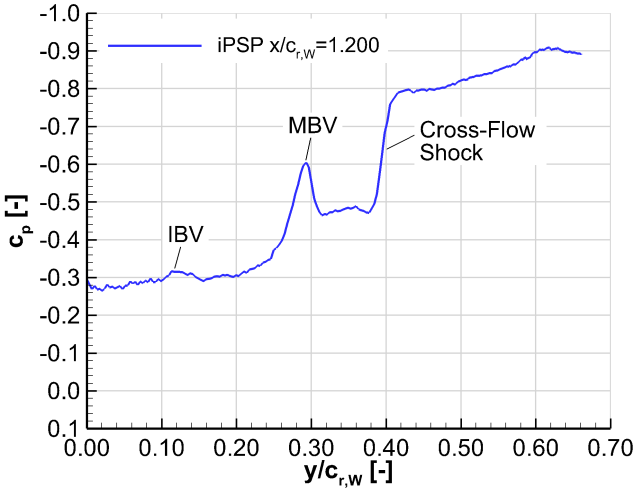

(d) Pressure section $x/c_{r,W} = 1.200$

Figure 16 – Surface pressure sections for $Ma_\infty = 1.15$ and $Re_{l_\mu} = 3.27 \times 10^6$ at $\alpha = 12^\circ$

In Fig. 13a, a so-called rear or terminating shock appears close to the trailing edge. This shock, also described in the literature as a trailing-edge shock, can be attributed to the upstream effects of

the trailing edge, where the Kutta condition must be fulfilled [29]. In order to return to free stream conditions, the flow has to decelerate near the trailing edge, and a normal shock will be formed that terminates the region with supersonic flow. In the evaluation of the local Mach number in Fig. 14, it can also be observed that the flow is decelerated to subsonic speeds. Fig. 13b shows that the position of the trailing-edge shock is exposed to strong fluctuations in the chordwise direction. The shock front of the trailing-edge shock is significantly curved in the spanwise direction. A strong curvature can be observed in the area of the vortex-shock interaction with the MBV at $x/c_{r,W} = 1.420$ and $y/c_{r,W} = 0.290$.

Figure 15a shows the surface traces of the vortex trajectories of the IBV and the MBV, and Fig. 15a shows the pressure distribution along the vortex trajectories. Compared to the subsonic and transonic flow conditions, no vortex interactions between the IBV and the MBV can be observed in the supersonic case. In the pressure distribution, the vortex-shock interaction of the second normal shock and the third normal shock can be identified by a moderate increase in pressure. The respective positions of the vortex-shock interactions of the second and the third normal shock between the IBV and the MBV are shifted due to the normal shocks oriented in an angular direction, according to Fig. 13a. The vortices recover after passing these two shocks, and no shock-induced vortex breakdown can be observed. In the trailing edge section, there is a strong interaction with the previously mentioned trailing edge shock. In the trailing edge section, there is a strong vortex-shock interaction for both the IBV and the MBV with the described trailing-edge shock. The pressure ratios $c_{p,pre}/c_{p,post}$ for the trailing edge shock are 2.24 for the IBV and 2.10 for the MBV.
In pressure section S_1 according to Fig. 16a, the position and the pressure level of the suction peak of the IBV from the iPSP measurements ($y/c_{r,W} = 0.567$) at $y/c_{r,W} = 0.089$ correspond with the transient pressure transducers. The pressure distribution shows the presence of a cross-flow shock in the area of the vortex core of the MBV. The pressure gradient due to the cross-flow shock is indicated both in the pressure distribution of the iPSP measurements and in the transient pressure transducers. In pressure section S_2 according to Fig. 16b, the pressure difference due to the cross-flow shock is significantly increased compared to pressure section S_1. In pressure section $x/c_{r,W} = 0.900$ in Fig. 16c, a second cross-flow shock between $y/c_{r,W} = 0.318$ and $y/c_{r,W} = 0.335$ can be observed in addition to the first cross-flow shock. The suction peak of the partially developed OBV is located at a spanwise position of $y/c_{r,W} = 0.335$. In the pressure section $x/c_{r,W} = 1.200$, shown in Fig. 16d, the suction peak of the IBV is located at $y/c_{r,W} = 0.116$ and the pronounced suction peak of the MBV is positioned at $y/c_{r,W} = 0.295$. The second cross-flow shock is located at $y/c_{r,W} = 0.400$. As previously discussed, no pronounced OBV suction peak has been developed for this supersonic flow case, and therefore no pronounced suction peak can be detected.

5. Conclusion

In this study, fast-response pressure-sensitive paint measurements (iPSP) for the analysis of the surface pressure distributions and pressure fluctuations on the hybrid-delta wing of the DLR-F23 configuration are performed at the Transonic Wind Tunnel Göttingen (DNW-TWG). The half-span wind tunnel model consists of a triple-delta-wing planform with a leading-edge sweep of $\varphi_{W,1} = 45^\circ$ at the LEVCON, $\varphi_{W,2} = 75^\circ$ at the strake, and $\varphi_{W,3} = 45^\circ$ at the main wing section and an ogival cosine-chined forebody. The experimental investigations are conducted in a Mach number range from $Ma_\infty = 0.55$ to $Ma_\infty = 1.15$ for angles of attack between $\alpha = 0^\circ$ and $\alpha = 30^\circ$. The Reynolds number related to the mean aerodynamic chord is in the range of $2.35 \times 10^6 < Re_{l_\mu} < 3.27 \times 10^6$. The time-resolved iPSP measurements, recorded at a frame rate of 3200 Hz, are validated with 75 unsteady pressure transducers arranged in three spanwise aligned pressure sections on the upper side of the wing.
The analysis focuses on three selected flow conditions in the subsonic, transonic, and supersonic speed range with regard to vortex-vortex and vortex-shock interactions as well as vortex breakdown. For the investigation of these complex flow phenomena, the surface traces of the primary vortex trajectories and the pressure distributions along the vortex trajectories are evaluated. For the subsonic flow case at $Ma_\infty = 0.65$ and an angle of attack of $\alpha = 18^\circ$, the traces of the primary vortex trajectories

of the inboard-vortex (IBV), the midboard vortex (MBV) and the outboard vortex (OBV) can be identified. A strong interaction between the IBV and the MBV is observed and results in vortex merging at $x/c_{r,W} = 0.960$. The mechanism of vortex merging involves the exchange of momentum and energy, stabilizing the MBV. The vortex bursting location of the MBV can be observed further downstream at $x/c_{r,W} = 1.16$ and of the OBV at $x/c_{r,W} = 1.20$. For the transonic flow case at $Ma_\infty = 0.85$ and $\alpha = 21°$, vortex-shock interactions can be identified. The first normal shock is positioned at $x/c_{r,W} = 0.725$ and causes a weak vortex-shock interaction with the IBV and the MBV. The second normal shock is located downstream at $x/c_{r,W} = 0.980$ and induces a strong vortex-shock interaction with the IBV and the MBV due to the high adverse pressure gradient. This interaction results in a shock-induced vortex breakdown of the IBV at $x/c_{r,W} = 1.02$, and of the MBV at $x/c_{r,W} = 1.06$. The Proper Orthogonal Decomposition (POD) method reduces the high-dimensional iPSP data into a series of orthogonal modes arranged according to their energy content. The first POD mode indicates the shock-induced vortex breakdown as the most energetic flow structure.
The supersonic flow case at $Ma_\infty = 1.15$ and $\alpha = 21°$ is characterized by compressible flow phenomena and vortex-shock interactions. In the area of the outboard main wing, supersonic local Mach numbers of $Ma = 2.00$ to $Ma = 2.60$ are observed. A cross-flow shock in the direction of the vortex core of the MBV can be identified. These shocks are positioned along the primary vortex for transonic and supersonic flow conditions. A second cross-flow shock forms at the kink to the main wing and forms along the partially developed OBV. In the area of the trailing edge, a trailing-edge shock appears, which leads to a strong adverse pressure increase.

In order to enhance the analysis of the unsteady aerodynamics, a spectral analysis of the time-resolved iPSP data is intended. The frequency information for unsteady flow phenomena can be determined based on the proposed evaluation of the Power Spectral Density (PSD) of the iPSP measurement data. For the investigation of the flow field and the vortex trajectories, the evaluation of the stereo-PIV measurements on the DLR-F23 configuration is planned. Furthermore, the present experimental results provide validation data for scheduled CFD simulations for transonic and supersonic flow conditions.

6. Contact Author Email Address

patrick.hartl@dlr.de

7. Acknowledgements

The authors gratefully acknowledge that this work could be conducted within the DLR project Diabolo, funded by the Federal Office of Bundeswehr Equipment, Information Technology and In-Service Support (BAAINBw). The authors would like to express their sincerest gratitude to the scientific and technical staff of the Department of Aeroelastic Experiments at the DLR Institute of Aeroelasticity, namely Ms. A. Altkuckatz, Mr. H. Böhlken, Mr. T. Büte, and Mr. H. Ernst, without whom the experimental investigation of the DLR-F23 configuration would not have been feasible. The first author would especially like to thank Mr. T. Schmidt for the fruitful scientific discussions and the proofreading of this paper. Furthermore, a special thanks goes to Mr. U. Henne and Mr. C. Klein from the Department of Experimental Methods at the DLR Institute of Aerodynamics and Flow Technology. Finally, the authors would like to thank the team of the Transonic Wind Tunnel Göttingen (TWG) of the German-Dutch Wind Tunnel (DNW), namely Mr. M. Bruse as head of the TWG and Mr. A. Benkel as the responsible project manager, for their support in the experimental measurements.

8. Copyright Statement

References

[1] Hövelmann A, Pölzlbauer P, Pfnür S, Winkler A, and Hitzel S M. Hybrid-Delta Wing Simulations – Industrial Application for Combat Aircraft Design. *AIAA Science and Technology Forum and Exposition, AIAA SciTech Forum 2022*, pages 1–18, 2022.

[2] Hitzel S M, Winkler A, and Hövelmann A. Vortex Flow Aerodynamic Challenges in the Design Space for Future Fighter Aircraft. *Notes on Numerical Fluid Mechanics and Multidisciplinary Design*, 142:297–306, 2020.

[3] Werner M, Henne U, Rein M, and Richter K. Vortex Interactions above Multi-Swept Wing Planforms at Transonic Speeds. *AIAA Science and Technology Forum and Exposition, AIAA SciTech Forum 2024*, 2024.

[4] Schiavetta L A, Boelens O J, Crippa S, Cummings R M, Fritz W, and Badcock K J. Shock Effects on Delta Wing Vortex Breakdown. *Journal of Aircraft*, 46(3):903–914, 2009.

[5] Lambourne N C and Bryer D W. The Bursting of Leading-Edge Vortices-Some Observations and Discussion of the Phenomenon. *Aero. Res. Counc.*, (3282):1–35, 1962.

[6] Lucca-Negro O and O'Doherty T. Vortex Breakdown: A Review. *Progress in Energy and Combustion Science*, 27(4):431–481, 2001.

[7] Gursul I. Recent Developments in Delta Wing Aerodynamics. *Aeronautical Journal*, 108(1087):437–452, 2004.

[8] Zastrow J. Design of Aeroelastic Wind Tunnel Experiments on Vortex Induced Effects on Multi-Delta Wings. *Deutscher Luft- und Raumfahrtkongress 2018*, 2018.

[9] Zastrow J. Characterizing a multi delta wing for aeroelastic wind tunnel experiments. *International Forum on Aeroelasticity and Structural Dynamics 2019, IFASD 2019*, pages 1–14, 2019.

[10] Klein C, Engler R H, Henne U, and Sachs W E. Application of Pressure-Sensitive Paint for Determination of the Pressure Field and Calculation of the Forces and Moments of Models in a Wind Tunnel. *Experiments in Fluids*, 39(2):475–483, 2005.

[11] Ponomarev S and Gouterman M. Fast Responding Pressure Sensitive Paints based on High Concentration of Hard Particles in Polymer. *Proceedings of the 6th Annual Pressure-Sensitive Paint Workshop*, 1998.

[12] Gregory J W, Sakaue H, and Sullivan J P. Unsteady Pressure Measurements in Turbomachinery Using Porous Pressure Sensitive Paint. *40th AIAA Aerospace Sciences Meeting and Exhibit*, (January), 2002.

[13] Gregory J W, Asai K, Kameda M, Liu T, and Sullivan J P. A Review of Pressure-Sensitive Paint for High-Speed and Unsteady Aerodynamics. *Proceedings of the Institution of Mechanical Engineers, Part G: Journal of Aerospace Engineering*, 222(2):249–290, 2008.

[14] Kameda M, Tabei T, Nakakita K, Sakaue H, and Asai K. Image Measurement of Unsteady Pressure Fluctuation on a Delta Wing by an Anodized Aluminum PSP. *ICIASF Record, International Congress on Instrumentation in Aerospace Simulation Facilities*, 2005:181–188, 2005.

[15] Wiggen S, Henne U, Klein C, Nuhn J, and Sachs W. Unsteady Surface Pressures Measured at a Pitching Lambda Wing with Vortex Dominated Flow and Transonic Effects. *CEAS Aeronautical Journal*, 9(3):417–427, 2018.

[16] Katzenmeier L, Hilfer M, Stegmüller J, and Breitsamter C. Application of Fast-Response Pressure Sensitive Paint to Low-Speed Vortical Flow at High Angles of Attack. *Experiments in Fluids*, 64(10):1–20, 2023.

[17] Berkooz G, Holmes P, and Lumley J L. The Proper Orthogonal Decomposition in the Analysis of Turbulent Flows. *Annual Review of Fluid Mechanics*, (25):539–575, 1993.

[18] Cordier L and Bergmann M. Proper Orthogonal Decomposition: An Overview. *VKI Lecture Series 2003-04*, 2003.

[19] Wiggen S and Voß G. Development of a Wind Tunnel Experiment for Vortex Dominated Flow at a Pitching Lambda Wing. *CEAS Aeronautical Journal*, 5(4):477–486, 2014.

[20] Gößling J, Ahlefeldt T, and Hilfer M. Experimental Validation of Unsteady Pressure-Sensitive Paint for Acoustic Applications. *Experimental Thermal and Fluid Science*, 112:109915, 2020.

[21] Puklin E, Carlson B, Gouin S, Costin C, Green E, Ponomarev S, Tanji H, and Gouterman M. Ideality of Pressure-Sensitive Paint. I. Platinum Tetra(pentafluorophenyl)porphine in Fluoroacrylic Polymer. *Journal of Applied Polymer Science*, 77(13):2795–2804, 2000.

[22] Tianshu L, Sullivan J P, Asai K, Klein C, and Egami Y. *Pressure and Temperature Sensitive Paints*. Experimental Fluid Mechanics. Springer International Publishing, Cham, 2021.

[23] Verhaagen N G and Maseland J E J. Investigation of the Vortex Flow over a 76/60-deg Double Delta

Wing at 20 deg Incidence. *9th Applied Aerodynamics Conference, 1991*, 1991.

[24] Hummel D and Brennenstuhl U. Vortex Formation over Double-Delta Wings. *13th ICAS Congress*, 1982.

[25] Delery J M. Aspects of Vortex Breakdown. *Progress in Aerospace Sciences*, 30(1):1–59, 1994.

[26] Stanbrook A and Squire L C. Possible Types of Flow at Swept Leading Edges. *Aeronautical Quarterly*, 15(1):72–82, 1964.

[27] Rein M. Subsonic, Transonic and Supersonic Wind Tunnel Tests of the Generic Slender Wing Configuration DLR F22 with Leading-Edge Vortex Controllers and Strakes. Technical report, German Aerospace Center (DLR), Institute of Aerodynamics and Flow Technology, Göttingen, Germany, 2022.

[28] Squire L C. Leading-Edge Separations and Cross-Flow Shocks on Delta Wings. *AIAA Journal*, 23(3):321–325, 1985.

[29] Elsenaar A and Hoeijmakers H W M. An Experimental Study of the Flow over a sharp-edged Delta Wing at Subsonic and Transonic Speeds. *AGARD-CP-496*, page 20, 1990.

[30] Brodetsky M D, Kharitonov A M, Krause E, Pavlov A A, Nikiforov S B, and Shevchenko A M. Supersonic Leeside Flow Topology on Delta Wings. *Experiments in Fluids*, 29(6-6):592–604, 2000.